Review article

Open Access

Daan Martens* and Peter Bienstman

Comparison between Vernier-cascade and MZI as transducer for biosensing with on-chip spectral filter

Abstract: The Mach-Zehnder interferometer (MZI) and the Vernier-cascade are highly responsive photonic sensors with large design freedom. They are therefore very suitable for interrogation through a broadband source and an on-chip spectral filter, a sensing scheme that is well equipped for point-of-care applications. In this work, the MZI is shown to outperform the Vernier-cascade through a better minimum detectable wavelength shift as well as a higher power efficiency, indicating its superiority in this sensing scheme. Fabricated MZIs yield bulk detection limits down to 8.8×10^{-7} refractive index units (RIU) in a point-of-care compatible measuring setup, indicating the potential of the proposed sensing scheme.

Keywords: integrated photonics; photonic sensing; point-of-care sensing; Mach-Zehnder interferometer; Vernier-cascade.

1 Introduction

Label-free integrated evanescent field photonic biosensors are seen as very promising candidates for real-time qualitative and quantitative measurements on biological systems. In these sensors, a change in effective refractive index caused by an analyte is typically converted into a measurable quantity, most commonly a resonant wavelength shift, through an integrated photonic transducer.

*Corresponding author: Daan Martens, Photonics Research Group, INTEC, Ghent University – IMEC Center for Nano- and Biophotonics (NB-Photonics), Ghent University, Ghent, Belgium, e-mail: daand.martens@ugent.be
Peter Bienstman: Photonics Research Group, INTEC, Ghent University – IMEC Center for Nano- and Biophotonics (NB-Photonics), Ghent University, Ghent, Belgium

Various types of sensors have been developed: Young and Mach-Zehnder (MZI) interferometers, bimodal sensors, ring resonators, photonic crystal sensors and various others [1–4]. In general, these sensors provide sensitivity, selectivity and versatility, which renders them applicable in a broad range of disciplines, ranging from medicine over food quality control to environmental managing. Furthermore, they offer great potential as lab-on-a-chip devices, performing point-of-care measurements at an affordable cost.

While practical applications have emerged [5–7], their breakthrough has been limited by the necessity of either an expensive tunable laser or an off-chip spectrometer in the readout instrument, making them expensive and/or slow. Therefore, the instrumentation cost is typically high, rendering the system unfit for true point-of-care applications. We aim to overcome this important barrier by using a broadband light source in combination with an on-chip spectral filter as interrogation mechanism [8, 9]. The filter divides the transducer spectrum into different wavelength channels with spatially separated output ports. By fitting a curve to this dataset, the central wavelength of the original sensor spectrum is determined with an accuracy that surpasses the resolution of the spectral filter itself by multiple orders of magnitude. Nevertheless, the fitting accuracy, expressed as a minimum detectable wavelength shift, is typically lower than an interrogation through a tunable laser, which offers a narrow wavelength sweep at high power levels. As such, in order to maintain a low detection limit, a very sensitive transducer is required, which additionally needs to have a sufficiently broad spectrum to be resolvable by an on-chip spectral filter. The conventional ring resonator does not meet these criteria, as its sensitivity is simply the ratio of the wavelength to the group index and as such cannot be widely tuned. In [10], we proposed the Vernier-cascade, consisting of two such ring resonators in a series connection, as a sensor. It is suitable for this interrogation scheme, as its sensitivity and spectral period can be freely tuned through design, as we will show in this work. Here we will compare

this Vernier-cascade sensor with the MZI as a transducer, which exhibits very similar properties, as we will also show. The MZI has a long-standing tradition as an integrated photonic biosensor in various wavelength ranges and material platforms [11–17], including in Si_3N_4 [18, 19] which we will use for our fabricated devices. The Vernier has been used in sensing applications as well [20–24]. To our knowledge, neither has so far been used in combination with an on-chip spectral filter, apart from the Vernier sensor in our earlier work [9, 10].

First, we discuss the similarity of the sensors in terms of spectral period and peak shift under a change in effective index of the sensing element. Second, we discuss the best possible fit function for both types. Third, we compare the attainable limit of detection once the signals are sampled with the on-chip spectral filter. Noise is also added to the spectra to simulate a more realistic measurement environment. These simulations show that the MZI can reach lower detection limit and therefore is the better choice as a photonic transducer. To conclude, experimental results of the MZI sensor in a point-of-care compatible measurement setup are shown, attaining a detection limit comparable to integrated photonic sensors using a tunable laser or an off-chip spectrometer.

2 Theoretical analysis of the sensors

As shown in Figure 1A, the Vernier-cascade sensors consist of two ring resonators in a series configuration. One ring, the sensing ring, is exposed to the analyte, while the other, the reference ring, is isolated from it through a cladding. As such, the effective index of the waveguides of the respective rings is different. An

extensive theoretical analysis of the spectral characteristics of the Vernier-cascade sensor was carried out by Claes et al. [10]. If the difference in free spectral range (FSR) between the rings is small compared to the full-width at half-maximum of the resonances of the individual rings, the spectrum of their Vernier-cascade consists of an envelope function spanning multiple constituent peaks. Such a small difference in FSR is achieved by adapting the roundtrip lengths of the respective rings. An example of a spectrum for which this condition is met is given in Figure 2. The spectral period of the envelope function is then given by [10]

$$p_{env} = \frac{FSR_{sens} \cdot FSR_{ref}}{|FSR_{sens} - FSR_{ref}|} \tag{1}$$

where FSR refers to the free spectral ranges of the individual ring resonators. This can be rewritten as

$$p_{env} = \frac{\lambda_p^2}{|L_{sens}n_{g,sens} - L_{ref}n_{g,ref}|} \tag{2}$$

where n_g is the group index, λ_p is the peak wavelength and L is the roundtrip length. The tracked quantity in a sensing experiment with such a structure is the peak wavelength of the envelope, which has a strongly increased sensitivity in comparison with the individual peaks, due to the Vernier effect. The sensitivity of this envelope peak wavelength is given by [10]

$$\Delta\lambda_p = \frac{FSR_{ref}}{FSR_{ref} - FSR_{sens}} \frac{\Delta n_{eff,sens}\lambda_p}{n_{g,sens}} \tag{3}$$

where $\Delta n_{eff,sens}$ represents the change in effective index of the sensing arm, caused by a change in bulk index of the surrounding medium or a binding event. This can be rewritten as
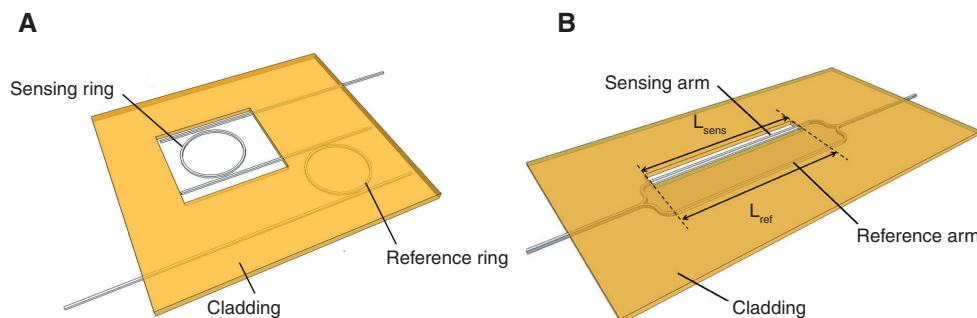
Figure 1: Schematic of both sensor types. In fabricated devices, waveguides can be curled into a spiral to limit the footprint, as shown in Figure 9.
(A) Vernier-cascade (B) Mach-Zehnder interferometer.

$$\Delta\lambda_p = \pm p_{\mathrm{env}} \frac{L_{\mathrm{sens}} \Delta n_{\mathrm{eff,sens}}}{\lambda_p} \qquad (4)$$

On the other hand, the MZI is already well documented; it is made up of a waveguide split into two separate waveguides, then the light in each arm travels a potentially different length, after which the signals are recombined, as shown in Figure 1B. Similar to the Vernier, the sensing arm is exposed to the analyte, while the reference arm is isolated from it through a cladding. As such, the arms can have different lengths as well as different refractive indices. The spectral period of the MZI is given by [1]

$$p_{\mathrm{env}} = \frac{\lambda_p^2}{|\, L_{\mathrm{sens}} n_{g,\mathrm{sens}} - L_{\mathrm{ref}} n_{g,\mathrm{ref}} \,|} \qquad (5)$$

where L is the arm length. This is completely equivalent to Eq. (2), if the arm length is substituted by the roundtrip length. Likewise, if dispersion is ignored, the sensitivity can be written as

$$\Delta\lambda_p = \pm p_{\mathrm{env}} \frac{L_{\mathrm{sens}} \Delta n_{\mathrm{eff,sens}}}{\lambda_p} \qquad (6)$$

This is again equivalent to the case of the Vernier (Eq. (4) upon substitution of the roundtrip length by the arm length. Figure 2 shows the spectra of a Vernier sensor and a MZI when the roundtrip lengths of the former match the arm lengths of the latter. These equations also illustrate the design freedom of these sensors, as they imply that the spectral period and the sensitivity can be designed independently by tuning the arm/ring roundtrip lengths. For the Vernier, a larger sensitivity with the same envelope

period will result in a higher number of constituent peaks, while for the MZI, the spectral shape will be completely unaltered. These design characteristics makes them very suitable for the proposed sensing scheme, where the spectral period of the sensor needs to be adapted to the practically attainable characteristics of the on-chip spectral filter and very high sensibility is desirable to compensate the reduced fitting accuracy.

Altogether, these similarities justify the comparison between these two structures, as both their sensitivities and spectral periods are equal. Therefore, the only difference in detection limit, given by the ratio of the minimum detectable wavelength shift to this sensitivity, is given by the minimum detectable wavelength shift. This, for our case, is defined by the ability to fit a curve to the filter output data and determine the peak wavelength with high precision, potentially in the presence of noise.

3 Intrinsic curve fitting potential

For our purposes, the only relevance of the fitted curve is the accuracy with which it determines the peak central wavelength after the spectrum has been sampled by an on-chip spectral filter. Generally, however, the better the fit, the more accurate we will be able to determine the central wavelength. Therefore, we will first evaluate fitting both curves themselves, without involving the discretization imposed by the on-chip spectral filter. As a figure of merit for the fit, we will directly use the accuracy of the extracted peak wavelength.

First, the MZI is considered. As its spectral shape is simply a squared cosine, its spectrum is fully determined by its period, scaled by its amplitude. Therefore, any MZI
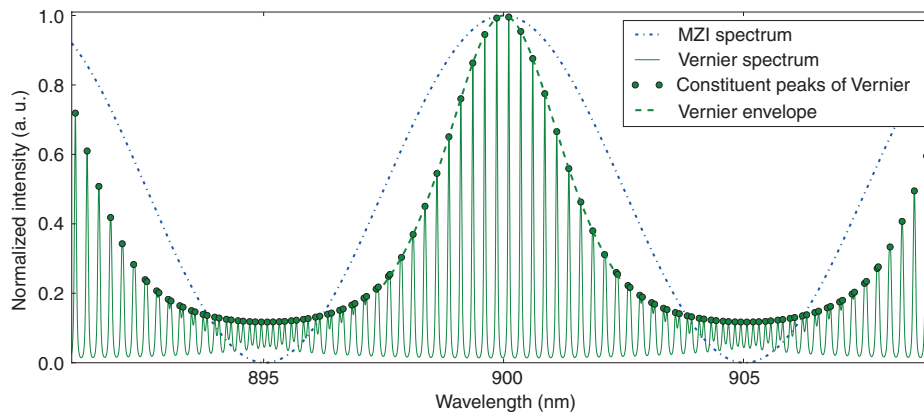
Figure 2: Spectra of a Vernier sensor and Mach-Zehnder interferometer, where the respective arms of the latter have the same length as the ring roundtrip of the former.

with the same spectral period trivially has the same spectral shape, irrespective of the arm lengths. For this shape, the squared cosine itself can be used as a fit function. Therefore, as far as the MZI is concerned, a fitting curve is available that represents the actual curve as accurately as possible.

For the Vernier, the situation is quite different. The function itself is not fitted, but rather its envelope spans all the constituent peaks, as shown in Figure 2. In the approach of [10] all individual ring resonant peaks are approximated by a Lorentzian through a first-order Taylor approximation. By further approximating the full widths at half maximum (FWHMs) of the rings as equal and neglecting the difference between the FSRs of the rings in comparison to their absolute value, the envelope of the constituent peaks is shown to be well approximated by a squared Lorentzian. The peak wavelength of this approximation corresponds with the peak wavelength of the envelope function. As this method to obtain this fit contains multiple approximations, the accuracy of this fit will be limited, especially off-peak, in contrast to the MZI where a perfect fit is available. The common figure of merit to describe such a fit accuracy is the minimum detectable wavelength shift, defined as three times the standard deviation on a set of fitted peaks on supposedly identical spectra, where the difference can arise from either fitting limitations or noise.

In comparison with the MZI, the Vernier spectrum is determined by numerous additional parameters, which makes it more complex but also more versatile. However, by making very minor approximations, the number of parameters on which the envelope of the Vernier spectrum depends can be reduced. If we assume the waveguides to be lossless, and all self-coupling coefficients τ which govern the coupling between the rings and the access waveguides [25] of the ring resonators to be equal, the Vernier spectrum is given by

$$T = \frac{(1-\tau^2)^4}{(1+\tau^4-2\tau^2\cos(C_1\nu))((1+\tau^4-2\tau^2\cos(C_2\nu))} \quad (7)$$

where ν is the frequency, $C_i = 2\pi n_i L_i/c$ with c the speed of light in vacuum, n_i the effective refractive index and L_i the roundtrip length of the respective ring resonators. The denominator can be rewritten as

$$2\tau^4[\cos((C_1-C_2)\nu)+\cos((C_1+C_2)\nu)]-4(\tau^6+\tau^2)$$
$$\cos\left(\frac{C_1+C_2}{2}\nu\right)\cos\left(\frac{C_1-C_2}{2}\nu\right)+\tau^8+2\tau^4+1 \quad (8)$$

This is only dependent on the roundtrip lengths through their weighted sum (C_1+C_2) or weighted difference

(C_1-C_2). For the envelope, which is the target of the fitting procedure, the high-frequency components will reach their extremes at $\cos((C_1+C_2)\nu)=\pm1$ and $\cos((C_1+C_2)\nu/2)=\pm1$, meaning that the envelope is only dependent on the lengths through their weighed difference $L_1n_1-L_2n_2$, which remains constant for any Vernier with the same FSR (Eq. (2)). Therefore, similar to the MZI, different roundtrip lengths will not influence the envelope spectrum at all, as long as the FSR remains the same. Furthermore since C_1-C_2 scales inversely with the FSR, a change in FSR simply results in a 'stretching' of the frequencies, implying that we can normalize all results with respect to the FSR. If we make the (typically small) assumption that roundtrip propagation losses in both rings are equal, losses can be included into Eq. (8) by simply substituting τ by $\tau\sqrt{A}$. There will be a change in amplitude as well, but this is inconsequential for the shape of the spectrum. In conclusion, the only parameter that influences the spectral shape of the envelope of the Vernier spectrum is the self-coupling coefficient τ.

In Figure 3 this minimum detectable wavelength shift per FSR of the sensor is plotted for the Vernier sensor. A parameter sweep was done for both the fraction of the FSR used in the fit as well as the number of points used. The location of the used points was randomized and averaged, by modification of the sensor lengths, shifting the location of the constituent peaks over the constituent peak spacing, while keeping the same FSR and envelope. This corresponds to a realistic situation, where, due to fabrication imperfections, we have no control over the exact locations of the constituent peaks. Neither losses nor noise were included, to assess the intrinsic accuracy of the fit. As a fit function, the squared Lorentzian proposed by Claes et al. [10] is used. The self-coupling coefficients
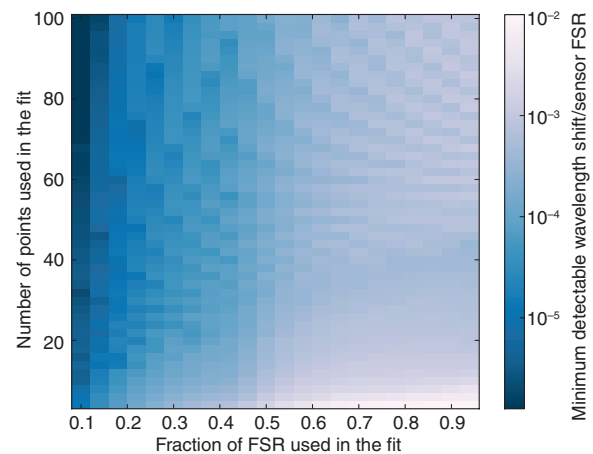

Figure 3: Minimum detectable wavelength shift of Vernier sensor per FSR in function of fraction of the FSR used and number of points used in fit.

of the ring resonators were chosen at 0.7, but the observed trends are valid for other values as well.

The results from these simulations indicate that with this fit, in a noiseless and lossless situation, the fit reaches an accuracy down to 10^{-5} times smaller than the FSR, if sufficient points are available close to the peak. This value could be improved even more by going closer to the peak, but this is not relevant for utilization in combination with an on-chip spectral filter. The main conclusion is that the fit quickly deteriorates once a large fraction of the FSR is included, due to reduced accuracy of the fitting function further away from the peak. There is also a small deterioration for a reduced number of points but much less severe. Despite these trends, even in the worst case, where only four points are used, spanning the whole FSR of the MZI, the accuracy of the fit is still 100 times smaller than the FSR of the sensor.

As described before, the presented results are valid for *any* Vernier with the same self-coupling coefficients, as these will have exactly the same envelope function. We can expect that Verniers with higher self-coupling coefficients will yield even better minimum detectable wavelength shifts, as they will have a sharper peak, due to the higher Q factor of the individual ring resonators. While this would be desirable to further optimize the intrinsic results, this is not compatible with the given sensing scheme, where on-chip spectral filters sample the spectrum. Apart from the availability of an adequate fitting function, there is another important property that determines the suitability of a sensor for the given sensing scheme: the total transmitted power. As the aim is to construct a point-of-care sensor, cost-efficiency is of the utmost importance, and a more power-efficient device can use a cheaper light source. The transmitted power of the Vernier will be substantially lower in comparison with the MZI, as the cascaded rings filter out most of the power. This can be clearly seen in Figure 2. The consequences of this are shown in Figure 4, where the ratio of transmitted power of the MZI to the Vernier within a single FSR is shown, for different self-coupling coefficients, as a function of sensing arm length in case of the MZI and ring roundtrip lengths in the case of the Vernier. Propagation losses of 1 dB/cm were added, as this is the typical order of magnitude for the material platform that will be used for fabrication [26].

Even for short sensors, where the propagation losses are negligible, the MZI is more power-efficient by a factor of five than the Vernier sensor with the lowest self-coupling coefficient, and the ratio increases by multiple orders of magnitude for higher τ values. For longer sensors, the effect is even more pronounced. This higher
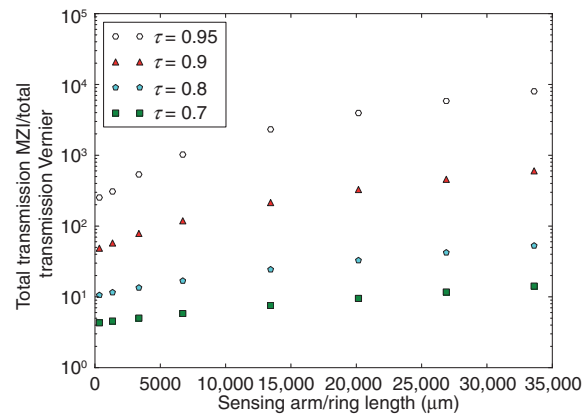
Figure 4: Ratio of total transmission within one FSR of the MZI to the Vernier. τ indicates the self-coupling coefficients of the Vernier sensor.

power efficiency is a fundamental advantage of the MZI in point-of-care applications.

# 4 Performance after sampling by an on-chip spectral filter

In this work, the aim is to use a broadband light source in combination with an on-chip spectral filter as a read-out mechanism. Therefore, while the intrinsic accuracy of the curve fitting sets an important upper limit on the precision, the true figure of merit of the described sensor is the precision with which a spectrum sampled by an on-chip spectral filter can be translated to a peak wavelength, as that will define the practical minimum detectable wavelength shift. This sampling procedure can be simulated by taking the convolution of the original spectrum of the sensor with a generic spectral filter channel, and then taking spectrally equidistant discrete points from the resulting curve as sampled spectrum to execute the fit on.

For the MZI, this sampling yields data exactly corresponding to the original curve. This can be understood as follows: If a normalized, perfect rectangular filter channel is assumed, an analytical solution of the convolution of the sensor spectrum with the filter spectrum is possible. In the frequency domain, this convolution yields

$$\text{MZI} * \acute{\text{o}} = 1 + \frac{2}{(C_1 - C_2)\Delta\nu}\sin\left(\frac{(C_1 - C_2)\Delta\nu}{2}\right)\cos((C_1 - C_2)(\nu - \nu_c))$$

$$(9)$$

where ν_c corresponds to the central frequency of the filter channel, $\Delta\nu$ is the spectral width of the channel, and C_i
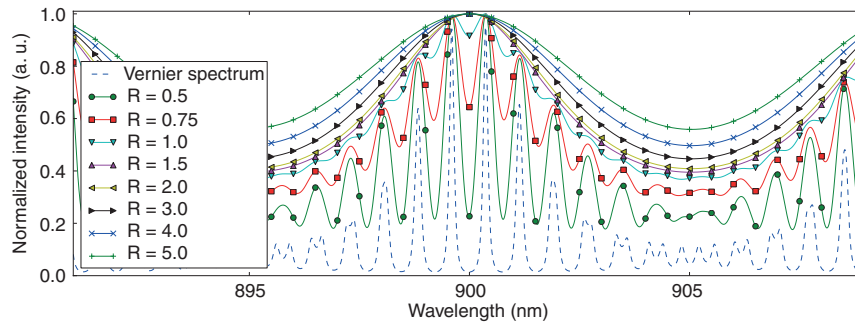
Figure 5: Convolution of Vernier spectrum with Gaussian channels of different width. R indicates the ratio of the filter channel width to the period of the constituent Vernier peaks.

equals $2\pi n_i L_i/c$, similarly to previous section but with L now the MZI arm length instead of roundtrip length. This has the same cosinusoidal shape as the original spectrum and can therefore be fitted perfectly with the same fit function. There is a reduction of the extinction ratio and this could come into play if noise is added, but in practice $\Delta\nu(C_1-C_2)$ will be very small, and the effect will typically be negligible. Hence, the original MZI spectrum is quasi exactly reproduced by the rectangular spectral filters. A similar conclusion holds for Gaussian filters, which approximate the channels of an on-chip arrayed wave-guide grating [8].

For the Vernier, on the other hand, such an analytical solution is not possible, but it is apparent that numerous difficulties arise to represent the envelope curve through filtering. In Figure 5 a Vernier spectrum is shown, convolved with rectangular channels with different widths. A relatively low number of constituent peaks was selected to illustrate that the constituent peaks are only sufficiently averaged out when the width of the channel is at least 1.5 times the period of the constituent Vernier peaks. Even if this condition is met, the spectral shape of the original envelope, in particular the extinction, is not completely retrieved, which impedes the fit.

To illustrate this, in Figure 6, the simulated minimum detectable wavelength shift is shown for the Vernier after sampling by a perfect Gaussian channel, as a function of both channel spacing and self-coupling coefficient. As the FWHM of the channel proved to have a negligible effect on the results, it was kept equal to the channel spacing for simplicity. A lengthy Vernier sensor with sufficient constituent peaks to ensure adequate averaging by the filter channels was selected. The central wavelengths of the filter channels were randomized with respect to the central wavelength of the sensor, over the used channel spacing, as in practice this relative position changes during a measurement. The filter channel spacing itself was not randomized, as it is highly reproducible in fabricated devices
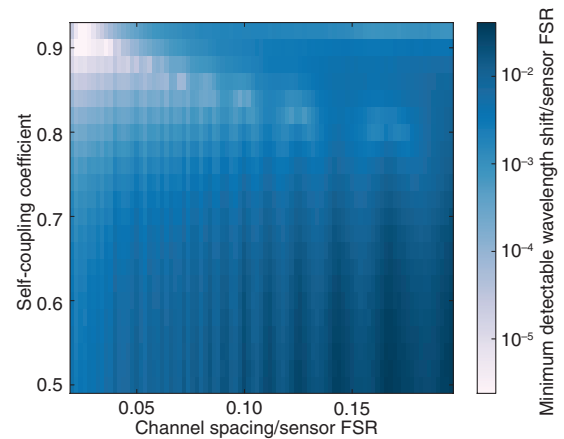
Figure 6: Minimum detectable wavelength shift on fitted wavelength for the Vernier as a function of ratio of filter channel width to sensor FSR and self-coupling coefficient.

[8]. No noise was added, to directly assess the effect of the filtering procedure.

For the channel spacing to sensor FSR ratio, a compromise has to be made between using a high number of points and using a small fraction of the FSR. Within the sweep used in Figure 6, the number of points is rather low, as it usually will be in practice. Therefore, the choice was made to include the full FSR in the fit. This means the used number of points is equal to the ratio of the FSR and the channel spacing.

The results of Figure 6 indicate that a smaller filter width and higher self-coupling coefficients are preferred, reaching a precision 10^{-5} times smaller than the spectral period of the sensor. For a bigger channel spacing, corresponding to a more coarse discretization, the optimum is not reached at the highest self-coupling coefficient but rather at intermediate values. The reason for this is that peaks with a high τ are sharper, and not enough points within the actual peak remain after a coarse discretization. This indicates that the optimal design of the Vernier

sensor depends on the characteristics of the spectral filter. Upon comparison of the data for $\tau = 0.7$ with the unfiltered data in Figure 3, it can be seen that the approximating character of the sampling deteriorates the minimum detectable wavelength by a factor 3–5. This indicates a loss in accuracy of fitting due to the inexact reconstruction of the envelope function through the spectral filters, in contrast with the MZI, where the original spectrum is reconstructed exactly.

5 Performance after addition of noise

In a realistic measuring environment, measurement noise will present. In this section, the sensor will be exposed to various levels σ of noise. For these simulations, a spectral filter with channel spacing of 1/10 the sensor FSR was selected, similar to what will be used in the fabricated devices in the next section. All 10 obtained points were used in the fit, as Figure 3 indicates that a fit of 10 points over the full FSR yields a similar result to 5 points over half the FSR and using a large number of points is expected to reduce the susceptibility to noise. The spectra were normalized after sampling by the spectral filter, as most noise sources will scale with the intensity. Both Vernier and MZI spectra were assumed lossless, and for the Vernier self-coupling coefficients of 0.7 and 0.9 were tested.

The results, given in Figure 7, show a linear curve for the MZI throughout the whole σ range, confirming that the fit can achieve arbitrary precision and is only limited by

the noise. For the Vernier, this is not the case, as there is a threshold under which the noise has no influence where the system is limited by the intrinsic fitting accuracy. This saturation level corresponds to the value found in Figure 6 and thus depends on the self-coupling coefficient, as illustrated here, as well as the ratio of the filter channel spacing to the FSR of the sensor.

In the regime where noise becomes the dominant limitation, the Vernier with self-coupling coefficients 0.9 briefly surpasses the MZI, before increasing very steeply for higher noise amplitudes. This is because a high self-coupling coefficient will result in a sharper spectrum, and it therefore can result in a more precise fit. For higher noise values, however, this sharpness becomes a drawback; because of the relatively high channel spacing of the spectral filter, most off-center points will 'drown' in noise. Because of this, the Vernier with lower self-coupling coefficients increases less dramatically for higher noise values but never surpasses the MZI.

From these simulations, it is clear that the optimal Vernier design will depend on numerous factors, including the expected noise as well as the spectral filter design. For very low noise levels, the MZI is very likely to outperform any Vernier, because of the inherent fit inaccuracy of the latter. For higher noise level, it is in principle possible for a well-designed Vernier sensor to slightly outperform an MZI, but the difference is limited. However, even in those cases, the MZI still seems the better choice for a point-of-care application, because it has a higher power efficiency, as described in Section 4. This low power efficiency is true in particular for Verniers with high self-coupling coefficients, which are required to surpass the MZI in terms of minimum detectable shifts.
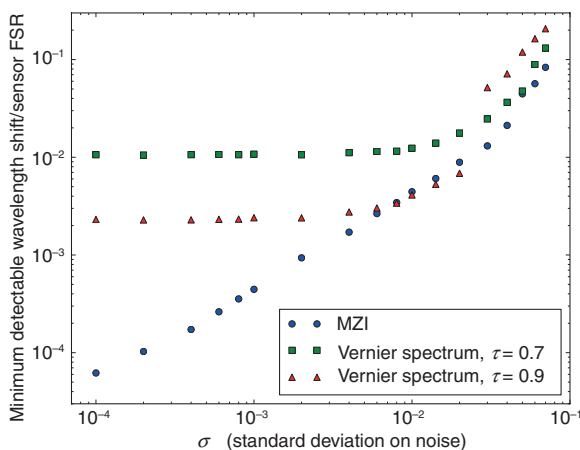
Figure 7: Minimum detectable wavelength shift for the MZI(circles) and the Vernier with self-coupling coefficients 0.7 (squares) and 0.9 (triangles) when noise is added.

6 Data averaging

These sensors were designed and optimized to be measured with an (on-chip) spectral filter. In this measurement scheme, there is no wavelength sweeping required and the channels of the on-chip spectral filter can be measured in parallel; thus, the only limiting factor on the measurement frequency is the speed of the camera or photodiodes that monitor the intensity of the outputs of the spectral filter. This means that data averaging to improve the minimum detectable wavelength shift will be possible in most practical applications. This is a non-trivial procedure, as averaging can be executed directly on the collected data, or on the obtained wavelengths after fitting. To examine this, a simulation was executed in which, each time, averaging
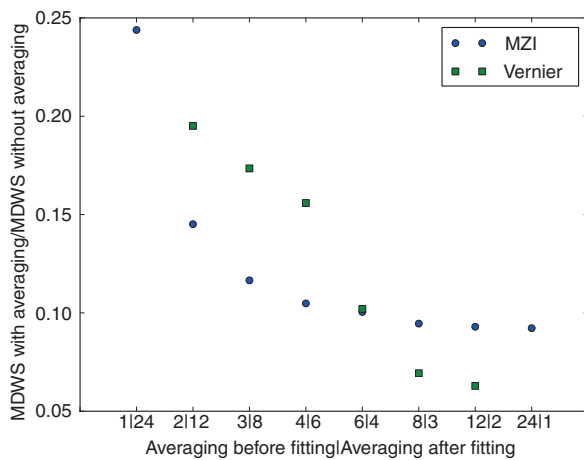
Figure 8: Minimum detectable wavelength shift (MDWS) improvement through averaging for the MZI (circles) and the Vernier (squares), all with averaging over 24 data points, spread out differently before versus after fitting the data.

was done over 24 noisy spectra, before or after the fitting. In Figure 8 the obtained improvement on the minimum detectable wavelength shift through averaging is shown. This graph primarily indicates that it is possible to improve the minimum detectable wavelength shift by over a factor 10 for both sensor types, further lowering the limit of detection. It also shows that it is more advantageous to average the raw data rather than the fitted results.

7 Experimental verification of MZI sensor in combination with an on-chip spectral filter

Sensors were fabricated in the novel Si_3N_4 material platform [26] to assess the practically reachable limit of detection and compare the technique with similar sensors. This material platform was selected because, in contrast to silicon-on-insulator, Si_3N_4 is transparent in the very near-infrared wavelength range where water absorption is lower and cheaper light sources and detectors are available in comparison with telecom range. The waveguides used in the sensors are rectangular, with a width of 700 nm and a height of 220 nm.

The used on-chip spectral filter was an arrayed waveguide grating with a channel spacing of 1 nm, as described in [8], where performance is shown to deteriorate for a smaller channel spacing in this material platform. Grating couplers [27] were used to couple light to and from the chip, at the input side through flood illumination of the chip surface with a freespace broadband source. An of-chip monochrome CMOS camera with a frame rate of 10 fps was used at the output side to monitor the intensity of the different channels of the spectral filter simultaneously. Similar to the material platform, these choices were made to ensure a point-of-care compatible sensing mechanism, as neither expensive optical components nor extremely high alignment precision is required.

Because both the on-chip spectral and the sensor themselves are rather spacious, only a limited sweep was implemented. Unfortunately, the fabricated Vernier sensors proved too power inefficient to perform a measurement, even when replacing the free-space source with a more efficient fiber-based equivalent. This confirms the observations made in section IV and means only MZI results are available from this material platform. A similar experiment in silicon-on-insulator with the Vernier sensor was performed by Claes et al. [10], resulting in a detection limit of 1.6×10^{-5} refractive index units (RIU).

Numerous fabricated MZI devices were characterized through bulk experiments, to assess the experimental minimum detectable wavelength shift and the detection limit. Similar to the aforementioned simulations, the minimum detectable wavelength shifts is conventionally defined as three times the standard deviation on the signal when no external changes are applied. Five of these sensors were measured in parallel, with a spectral period of 7 nm resulting in seven points per FSR which were all used in the fit. The sensing arm has a length of 1835 µm, and the reference arm measures 1912 µm. A microscopy picture of two of these sensors is shown in Figure 9.

The resulting sensorgram is shown in Figure 10. In this experiment, the sensor was exposed to increasing concentrations of HCl, alternated with water. The respective
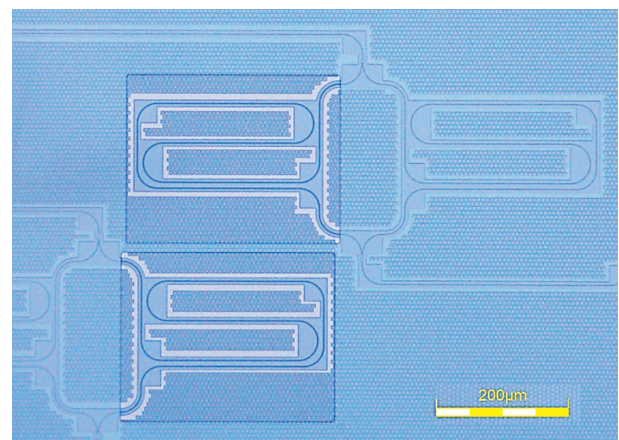
Figure 9: Microscopy picture of two MZIs. The arms are curled up to reduce the footprint of the sensor.
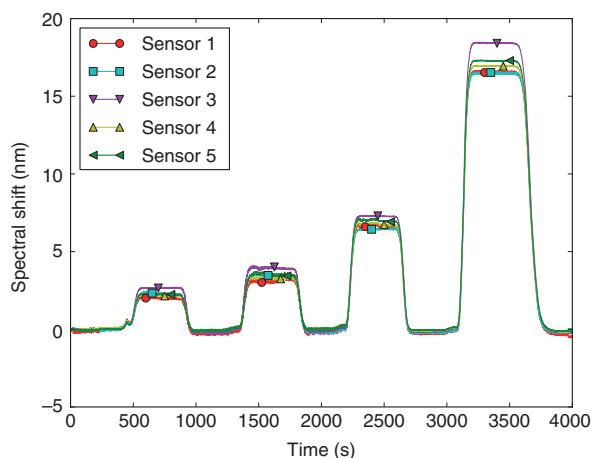
Figure 10: Sensorgram of parallel measurement of five MZI sensors, where the sensors are exposed to different concentrations of HCl in alternation with water.

concentrations of HCl were 0.05 M, 0.1 M, 0.2 M and 1 M, corresponding to effectice indices of 1.3331, 1.337, 1.3345 and 1.3408, respectively, in reference to the refractive index of water, 1.3328. Blood and urine, the most likely analytes in practical applications, have refractive indices of the same order [28].

After averaging over four data points, the minimum detectable wavelength shift for the five measured sensors was on average 13 pm. σ, measured as the average standard deviation on the measured intensity of a single spectral filter channel over time normalized by its amplitude was 0.02, in good agreement with the simulation in Figure 7.

In combination with the measured sensitivities on the order of 2100 nm/RIU this yields a detection limit around 6×10^{-6} RIU. Similar values were achieved numerous times, with an outlier of 8.8×10^{-7} RIU. These values are comparable with similar photonic sensors, most of which use more expensive readout mechanisms [1]. Moreover, the presented simultaneous measurement of five sensors indicates the ease of multiplexing. Also note that while it is a drawback for bulk sensing, the high-index-contrast material platform is particularly suitable for adlayer sensing. This indicates that this sensor comparatively will perform even better in surface sensitivity.

8 Conclusion

The MZI and Vernier sensor were proven equivalent in both spectral period and sensitivity, upon replacing the arm length of the former by the ring roundtrip of the latter, both compatible with cost-efficient interrogation through

a broadband source and an on-chip spectral filter. The capacity of both sensing mechanisms to precisely assess the peak wavelengths was investigated. For low noise levels, the MZI strongly outperforms the Vernier, as its sinusoidal spectrum can be fitted with infinite precision. In some cases with higher noise levels, a well-designed Vernier sensor can slightly outperform the MZI in terms of minimum detectable wavelength shift, but the latter still seems the better choice for interrogation through an on-chip spectral filter due to its much higher power efficiency. After fabrication, such a MZI in combination with an on-chip spectral filter yielded a detection limit comparable with sensing mechanisms with a more expensive interrogation mechanism, paving the way to numerous point-of-care applications.

References

[1] Gavela AF, García DG, Ramirez JC, Lechuga LM. Last advances in silicon-based optical biosensors. Sensors 2016;16:285.

[2] Liu L, Jin M, Shi Y, et al. Optical integrated chips with micro and nanostructures for refractive index and SERS-based optical label-free sensing. Nanophotonics 2015;4:419–36.

[3] Vollmer F, Yang L. Label-free detection with high-Q micro-cavities: a review of biosensing mechanisms for integrated devices. Nanophotonics 2012;1:267–91.

[4] Fan X, White IM, Shopova SI, Zhu H, Suter JD, Sun Y. Sensitive optical biosensors for unlabeled targets: a review. Anal Chim Acta 2008;620:8–26.

[5] Luchansky MS, Washburn AL, Martin TA, Iqbal M, Cary Gunn L, Bailey RC. Characterization of the evanescent field profile and bound mass sensitivity of a label-free silicon photonic microring resonator biosensing platform. Biosens Bioelectron 2010;26:1283–91.

[6] Bailey RC, Washburn AL, Qavi AJ, et al. A robust silicon photonic platform for multiparameter biological analysis. In: Proceedings of SPIE – The International Society for Optical Engineerings, Silicon Photonics IV, San Jose, CA: SPIE, 2009.

[7] Vörös J, Ramsden JJ, Csúcs G, et al. Optical grating coupler biosensors. Biomaterials 2002;23:3699–710.

[8] Martens D, Subramanian A, Pathak S, et al. Compact silicon nitride arrayed waveguide gratings for very near-infrared wavelengths. IEEE Photon Technol Lett 2015;27:137–40.

[9] Claes T, Bogaerts W, Bienstman P. Vernier-cascade label-free biosensor with integrated arrayed waveguide grating for wavelength interrogation with low-cost broadband source. Opt Lett 2011;36:3320–2.

[10] Claes T, Bogaerts W, Bienstman P. Experimental characterization of a silicon photonic biosensor consisting of two cascaded ring resonators based on the Vernier-effect and introduction of a curve fitting method for an improved detection limit. Opt Express 2010;18:22747–61.

[11] Heideman RG, Lambeck PV. Remote opto-chemical sensing with extreme sensitivity: design, fabrication and performance of a pigtailed integrated optical phase-modulated Mach-Zehnder interferometer system. Sens Actuator B Chem 1999;61:100–27.

[12] Brosinger F, Freimuth H, Lacher M, et al. A label-free affinity sensor with compensation of unspecific protein interaction by a highly sensitive integrated optical Mach-Zehnder interferometer on silicon. Sens Actuator B Chem 1997;44:350–5.

[13] Hong J, Choi JS, Han G, et al. A Mach-Zehnder interferometer based on silicon oxides for biosensor applications. Anal Chim Acta 2006;573:97–103.

[14] Kitsara M, Misiakos K, Raptis I, Makarona E. Integrated optical frequency-resolved Mach-Zehnder interferometers for label-free affinity sensing. Opt Express 2010;18: 8193–206.

[15] Luff BJ, Wilkinson JS, Piehler J, Hollenbach U, Ingenhoff J, Fabricius N. Integrated optical Mach-Zehnder biosensor. J Lightwave Technol 1998;16:583–92.

[16] Bruck R, Melnik E, Muellner P, Hainberger R, Lämmerhofer M. Integrated polymer-based Mach-Zehnder interferometer label-free streptavidin biosensor compatible with injection molding. Biosens Bioelectron 2011;26:3832–7.

[17] Dante S, Duval D, Fariña D, González-Guerrero AB, Lechuga LM. Linear readout of integrated interferometric biosensors using a periodic wavelength modulation. Laser Photon Rev 2015;9:248–55.

[18] Misiakos K, Raptis I, Salapatas A, et al. Broad-band Mach-Zehnder interferometers as high performance refractive index sensors: theory and monolithic implementation. Opt Express 2014;22:8856–70.

[19] Misiakos K, Raptis I, Makarona E, et al. All-silicon monolithic Mach-Zehnder interferometer as a refractive index and biochemical sensor. Opt Express 2014;22:26803–13.

[20] Boeck R, Flueckiger J, Yun H, Chrostowski L, Jaeger NAF. High performance Vernier racetrack resonators. Opt Lett 2012;37:5199–201.

[21] JinL, Li M, He J-J. Analysis of wavelength and intensity interrogation methods in cascaded double-ring sensors. J Lightwave Technol 2012;30:1994–2002.

[22] Jin L, Li M, He J-J. Highly-sensitive silicon-on-insulator sensor based on two cascaded micro-ring resonators with vernier effect. Opt Commun 2011;284:156–9.

[23] La Notte M, Passaro VMN. Ultra high sensitivity chemical photonic sensing by Mach-Zehnder interferometer enhanced Vernier-effect. Sens Actuator B Chem 2013;176:994.

[24] La Notte M, Troia B, Muciaccia T, Campanella CE, De Leonardis F, Passaro VMN. Recent advances in gas and chemical detection by Vernier effect-based photonic sensors. Sensors 2014;14:4831–55.

[25] Bogaerts W, De Heyn P, Van Vaerenbergh T, et al. Silicon microring resonators. Laser Photonics Rev 2012;6:47–73.

[26] Subramanian A, Neutens P, Dhakal A, et al. Low-loss singlemode PECVD silicon nitride photonic wire waveguides for 532–900 nm wavelength window fabricated within a CMOS pilot line. IEEE Photon J 2013;5:2202809.

[27] Subramanian A, Selvaraja S, Verheyen P, Dhakal A, Komorowska K, Baets R. Near-infrared grating couplers for silicon nitride photonic wires. IEEE Photon Technol Lett 2012;24:1700–3.

[28] El-Zaiat SY. Interferometric determination of refraction and dispersion of human blood-serum, saliva, sweat and urine. Opt Laser Technol 2003;35:55–60.